Dynamics and Stability Analysis of a Power System With a PMSG-Based Wind Farm Performing Ancillary Services

Gustavo Revel, *Member, IEEE*, Andres E. Leon, *Member, IEEE*, Diego M. Alonso, *Member, IEEE*, and
Jorge L. Moiola, *Senior Member, IEEE*

Abstract—This work studies the impact on power system dynamics of wind energy conversion systems based on permanent magnet synchronous generators when they perform ancillary services. The ability of modern variable-speed wind turbines to rapidly modify its active and reactive power is exploited in order to provide additional support to the power grid and enhance the overall stability of the system. A set of control loops are incorporated to the wind farm in order to achieve three supporting tasks: short-term frequency regulation, oscillation damping and voltage regulation. The analysis contemplates the effects of different loading conditions, measurement/communication time delays and control loop gains. Bifurcation diagrams, eigenvalue analysis and nonlinear time-domain simulations are used to assess the power system dynamics. The main contribution of this work is the assessment of wind farm ancillary services on the bifurcation structure of the power system.

Index Terms—Bifurcation analysis, oscillation damping, permanent magnet synchronous generators, power system dynamics, short-term frequency regulation, wind energy conversion systems.

I. INTRODUCTION

THE increasing penetration level of wind energy on the existing power networks, imposes new challenges to grid designers and operators. The behavior of these new generation centers is different from the classical ones, composed by large synchronous generators. The current wind energy conversion systems (WECSs) technologies use variable-speed turbines based on full-converter topologies, or doubly-fed induction generators [1]. The power electronic devices on these turbines, not only allow them to operate optimally for a wide range of wind speeds, but they can independently control their injected active and reactive powers. The later is useful for improving the overall system performance [2], [3].

A problem associated with high levels of wind energy penetration is the decrease in the frequency regulation capacity of the system. If all the WECSs act as independent active power sources they do not contribute to the total inertia of the system [4], and the network becomes less robust to perturbations, such as load variations and generation tripping. To overcome this problem, and to improve the stability margin of the system, dedicated control strategies for the WECS power converters can be designed. Several techniques consider the addition of a control action emulating the frequency droop of conventional generators [5]–[11]. These controllers exploit a fundamental property of the variable-speed wind farms: due to their power electronic devices, they can resort to the kinetic energy stored in their rotational masses faster than conventional generators. This stored energy is used to transiently support the system frequency. Once the transient event finishes, the wind farm ceases its participation and the power unbalance is compensated by the conventional synchronous generators. Then, to extract the maximum power available in the wind, the maximum power point tracker (MPPT) algorithm adjust the turbine speed according to the current wind velocity. The high controllability of the variable-speed wind turbines can improve other features of the power system, such as oscillations damping and voltage regulation. In this regard, [12], [13] investigate the damping of critical eigenvalues for different penetration levels, and the WECS contribution to diminish electromechanical oscillations.

The nonlinear nature of power systems, combined with the special features of WECS, drives the attention to investigate the dynamics from the nonlinear perspective. In this regard, bifurcation analysis provides a powerful tool to study the behavior of the power system under variations of parameters such as the load consumption level, generation dispatch, controllers gains, etc. The analysis of power system dynamics using bifurcation theory was explored in many articles over the last two decades [14]–[24], and it is currently used to investigate the dynamics of several power system components such as three-phase voltage source converters (VSC), dc-dc and flyback converters [25]–[29], photovoltaic systems [30] and permanent magnet synchronous motors [31].

In this work, bifurcation theory is used to investigate the dynamics of a power system including wind farms based on permanent magnet synchronous generators (PMSGs) when they perform ancillary control tasks such as short-term frequency regulation, inter-area oscillations damping, and voltage regulation. A two-area network model is considered, and three complementary controllers are included in the wind

farm. The methodology consists in a combination of nonlinear time-domain simulations, eigenvalue analysis and numerical continuations of the equilibria varying distinctive parameters, such as the loading factor, controller gains and time delays. The main objective is to analyze the effect on the dynamics after including ancillary services on the wind farm. The original bifurcation structure (without ancillary services) is compared with the one including the new capabilities on the WECS. The analysis helps in determining new stability/operational regions, revealing organizing centers of the dynamics and assessing the dynamical scenario for non-nominal operating conditions.

II. POWER SYSTEM MODEL

The power grid considered is the two-area system shown in the single-line diagram of Fig. 1. The system proposed in [32] for inter-area oscillation studies, is modified to include a 500 MVA wind farm in area #1. The parameter values of the grid and generators are obtained from [32, Example 12.6]. To use the standard numerical continuation package MatCont [33], the power system is modeled as a set of ordinary differential equations (ODE). Although restricting to ODE models is a limitation of the methodology, the package performs robust continuations with optimized algorithms, and brings valuable information about the bifurcations, such as the normal form coefficients that are used to classify the type of bifurcation and its unfolding. To obtain an ODE model for the entire power system, ODE representations of its components are derived. The synchronous generators are described by a fourth-order two-axis transient model, which accounts for the rotor mechanical and electrical dynamics. Automatic voltage regulators (AVR) and governors (GOV) are considered for all the machines. Power system stabilizers (PSS) are included in generators #1 and #3. The loads are composed by a ZIP model, i.e., a combination of constant impedance, current and power terms. The transmission lines are represented with π-models. Then, the entire model is assembled considering the dynamic equations of the bus voltages and the sum of the currents at the corresponding node. The variables of the transmission system are referred to a DQ synchronous reference frame, while the variables of the synchronous generators are expressed in their own reference frames. Therefore, a rotation matrix must be used to express the generator variables in the DQ synchronous reference frame, and vice versa. This transformation enables the connection between the differential equations of all synchronous generators and the electrical network. The procedure is explained in detail in [16], [34] and [35, Ch. 4]. The resulting ODE model has 64 state variables.

A. Wind Farm Model

The wind farm is connected to bus 7 on area #1 (see Fig. 1). It is represented by an aggregated model, describing a wind farm with several identical variable-speed PMSGs. The equivalent turbine is connected to the grid using a full converter topology, with two VSCs in back-to-back configuration. The WECS modeling and control strategies can be obtained from [1], [10]. In order to inject the maximum power available from the wind, the active power reference (p^{opt} in Fig. 2) is given by the MPPT strategy, based on the rotor speed measurement and the optimum power-speed cubic characteristic of the wind turbine [36], [37].
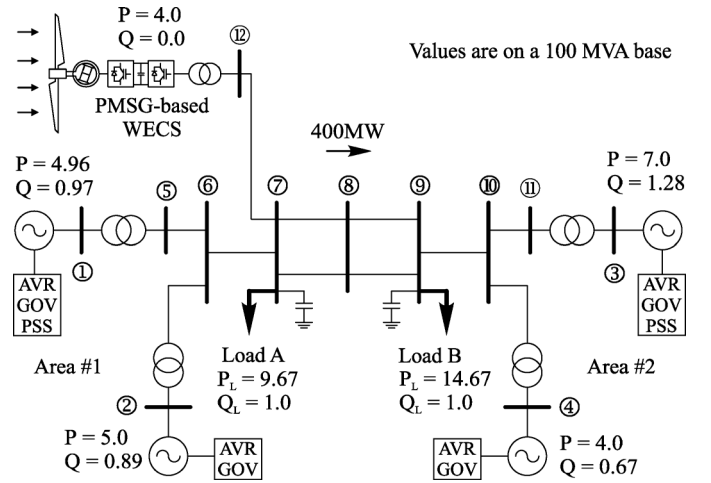

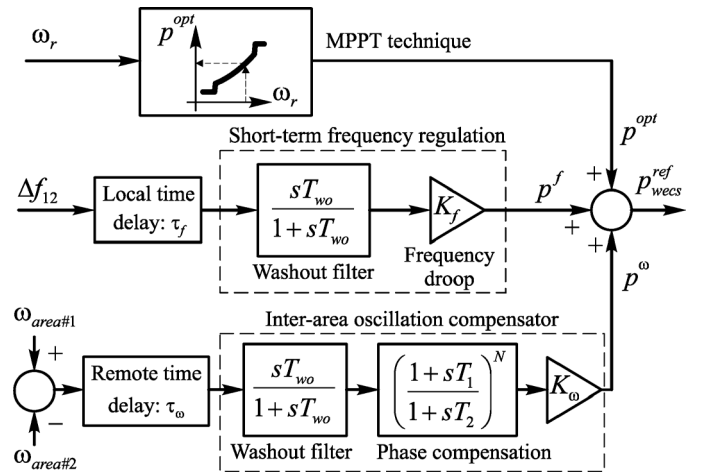Fig. 1. Single-line representation of the two-area multimachine power system.

Fig. 2. Supplementary controllers of WECS. Active power reference, including short-term frequency and oscillation damping compensators.

B. Ancillary Wind Farm Controllers

To include ancillary services into the wind farm, the active power reference p_{wecs}^{ref} has two additional terms: a short-term frequency regulation (p^f), and an inter-area oscillation damping (p^ω), as shown in Fig. 2. On the other hand, the WECS can also perform voltage support by means of reactive power injection through the voltage control loop.

1) Short-Term Frequency Regulation: The capability of modern wind farms to provide short-term frequency regulation is studied in [5]–[10]. In this paper the error signal is the frequency deviation on the point of common coupling (PCC), denoted as Δf_{12}. A time delay (τ_f), accounting for the local measure and internal control process, is included. A washout filter ensures that the wind farm only acts *transiently* on frequency regulation, allowing it to operate at the MPP on steady-state. The controller gain is defined as $K_f = A_t/R_f$, where the constant A_t accounts for the rated power of the wind farm and the base value of the per unit system (here $A_t = 5$), and R_f represents the *short-term droop* gain.

2) Inter-Area Oscillation Damping: The error signal is computed as the difference of representative measures of the frequency in each area, $\omega_{area\#1}$ and $\omega_{area\#2}$. A communication time delay (τ_ω) is considered. The effect of the remote time
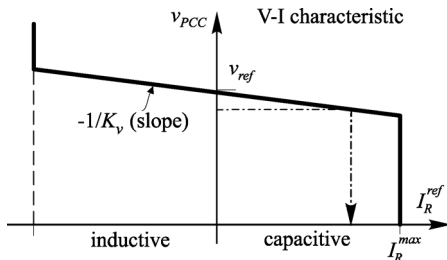
Fig. 3. V-I characteristic implemented by the voltage controller of the WECS.

delay become relevant due to the distance between the areas and the wind farm. Both, the local (τ_f) and remote (τ_ω) time delay blocks are modeled using a second-order Padé approximation [38], [39]. A washout filter is included to prevent the compensation in steady-state, and a phase compensator is added to improve the performance. Similar strategies are analyzed in [13], [40], [41] for different power systems and wind farm configurations.

3) Voltage Regulation: this controller monitors the voltage at PCC (v_{PCC}) and modifies the reactive current reference (I_R^{ref}) of the grid-side converter according to the voltage-current characteristic in Fig. 3 [42]. The gain K_v is tuned according to $K_v = A_t/R_v$, where A_t was defined previously and R_v represents the *voltage droop* gain. Voltage regulation schemes are described in [10], [43].

III. ANALYSIS OF THE DYNAMICS WITHOUT ADDITIONAL CONTROLLERS ON THE WECS

In this section, the WECS is considered as an independent power source, i.e., it injects the optimal active power without performing additional services on the power system. The dynamical behavior of the system with a constant wind velocity condition in the WECS is studied in terms of the loading scenario. Towards this end, variations of the loading factor of load B (at bus 9), denoted as α_B, are considered. The bifurcation diagram, obtained with the numerical continuation software package MatCont [33], is shown in Fig. 4(a). Parameter α_B is indicated on the abscissa, and the ordinate corresponds to the module of the voltage at bus 9 ($|V_9|$). Solid lines represent the stable equilibria, and dashed lines are the unstable ones. According to this diagram, the equilibrium point is stable for the nominal consumption $\alpha_B = 1$. When the loading factor is increased, the voltage on bus 9 decays until the equilibrium point becomes unstable due to a Hopf bifurcation H_1^+ for $\alpha_B = 1.296$. At this point a pair of complex conjugate eigenvalues of the linearization matrix crosses the imaginary axis. Then, the unstable equilibrium (dashed line) collapses in a saddle-node bifurcation, namely LP, for $\alpha_B = 1.34$. In this condition, the linearization of the system presents a real eigenvalue at the origin. For larger values of α_B neither stable nor unstable equilibria exist. The lower equilibrium branch, is always unstable and suffers a Hopf bifurcation at H_2^+.

A. Hopf Bifurcations and Limit Cycle Connections

The Hopf bifurcation H_1^+ is *subcritical* and, provided that some non-degeneracy conditions are satisfied [44], an unstable limit cycle emerges towards the left [as is depicted by the empty circles in Fig. 4(a)]. The stability of the cycle is determined by
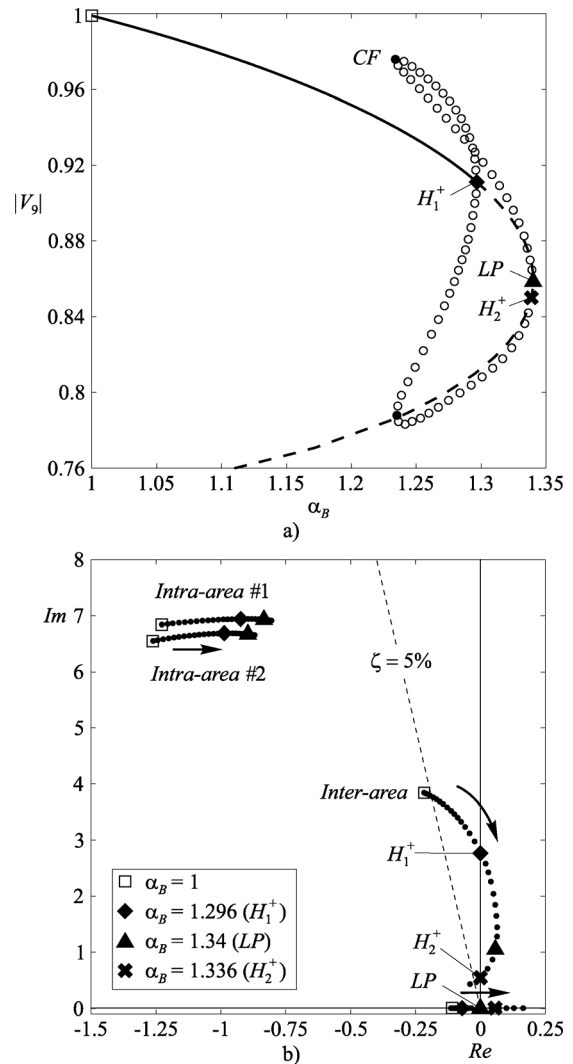

Fig. 4. Dynamics without additional controllers on the WECS. (a) Bifurcation diagram varying the loading factor α_B; (b) Loci of the relevant eigenvalues.

computing the coefficient of the normal form, known as *curvature index* or *Lyapunov index*[1]. For $\alpha_B > 1.296$, the system does not have any stable attractor (at least locally) resulting in voltage collapse. Therefore, the operation of the system is not possible beyond $\alpha_B > 1.296$. As is denoted by the superscript, the index of H_1^+ is positive. If the curvature index were negative, the Hopf bifurcation would be *supercritical*, and a stable limit cycle would grow toward the right. Notice that in this case, even though the equilibrium point would be unstable, the stable limit cycle would introduce a sustained oscillation. The sign of the curvature index was also studied for different levels of load A, wind speeds and values of the PSS gains. The first two cases modify the power transmitted from area #1 to area #2. As a general result, the inter-area mode becomes less damped when the power flow is increased. This phenomenon occurred either decreasing the load A or increasing the power injected by the wind farm. On the other hand, increasing the PSS gains moves the Hopf curve towards the saddle-node (stabilizing effect). In all the cases, the coefficient is positive leading to a subcritical Hopf

---

[1]The calculation of the curvature index requires the left and right eigenvectors and the derivatives of the vector field up to third order. The mathematical expression can be found in [44] and it is implemented in MatCont [33].

bifurcation H_1^+. Nevertheless, the coefficient has a small value (this explains that the unstable limit cycle grows abruptly near the bifurcation point) and it could become negative (supercritical) if other parameters were modified.

The unstable limit cycle born at H_1^+, grows towards the left until it undergoes a cyclic fold bifurcation (CF) for $\alpha_B = 1.235$. At this point, it collapses with the unstable cycle arising at the subcritical Hopf bifurcation H_2^+. For $\alpha_B < 1.235$, i.e., before CF, the basin of attraction of the stable equilibria (solid line) is restricted only by the manifolds of the unstable equilibria (dashed line). Therefore, a sufficiently large perturbation is required to drive the system out of its basin of attraction [45], [46]. The unstable cycle existing for $1.235 < \alpha_B < 1.296$, i.e., between CF and H_1^+, shrink further more the basin of attraction, therefore the stability may be lost for smaller perturbations.

B. Eigenvalue Analysis

The information about the local stability of the equilibria provided by the bifurcation diagram of Fig. 4(a), is in direct relation with the loci of the eigenvalues when α_B is varied. The loci of the critical eigenvalues is depicted in Fig. 4(b). They correspond to the so-called *inter-area* mode, representing the coupling between areas #1 and #2; the *intra-area* modes associated to the local oscillation modes of each area; and a real eigenvalue describing voltage collapse. The square markers in Fig. 4(b) indicate the eigenvalues location for $\alpha_B = 1$ (nominal operating point); the rhombi denote their position for $\alpha_B = 1.296$, i.e., when the Hopf bifurcation H_1^+ occurs (a pair of eigenvalues are on the imaginary axis); the triangles indicate the case for $\alpha_B = 1.34$, i.e., at the saddle-node bifurcation LP (one real eigenvalue is at the origin); and the crosses for $\alpha_B = 1.336$ corresponding to the Hopf bifurcation H_2^+.

An important fact to be noticed in the loci is that the damping of the inter-area mode decreases when the loading factor is increased. The Hopf bifurcations H_1^+ and H_2^+ correspond to the crossing of this mode over the imaginary axis, while the saddle-node bifurcation LP is produced by the crossing of the real eigenvalue through the origin.

IV. ANALYSIS OF THE DYNAMICS INCLUDING SHORT-TERM FREQUENCY REGULATION

In this section, the dynamics is analyzed when the active power reference of the WECS includes the short-term frequency compensator. In this analysis the inter-area oscillation damping controller as well as the voltage regulator are not activated. The effect of the short-term frequency regulator on the system dynamics, is studied performing a two-parameter continuation varying simultaneously the gain K_f and the load level α_B. Starting from the singular points found for $K_f = 0$, i.e., H_1^+, H_2^+ and LP in Fig. 4(a), the diagram of Fig. 5 is obtained. This two-parameter diagram represents the locus of the mentioned bifurcations and, for simplicity, the curves inherit the names from those in the one-parameter diagram.

The bifurcation diagram shows that when K_f is increased, the Hopf curves $H_{1;2}$ approach each other until they disappear for $K_f > 146.5$ as depicted in the blow-up of Fig. 6(a). This figure shows that both Hopf bifurcations ($H_{1;2}$) and the saddle-node bifurcation (LP) curves are organized by the
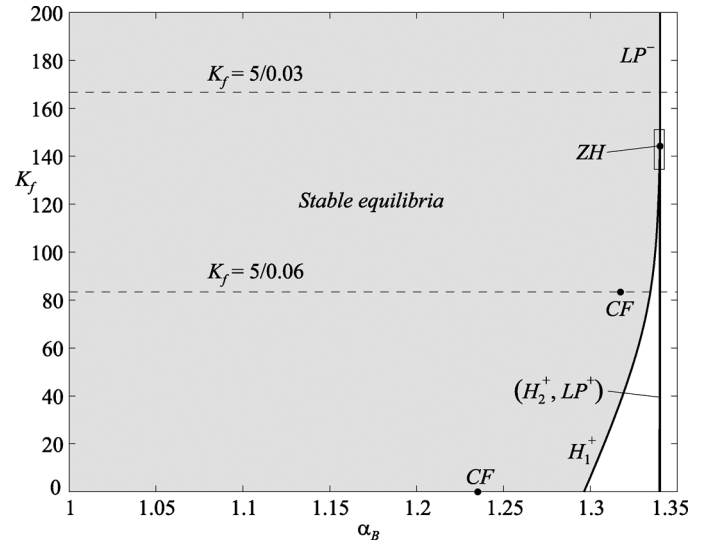

Fig. 5. Bifurcation diagram varying α_B and K_f simultaneously.

zero-Hopf bifurcation ZH. At this codimension-two singularity, the Hopf branches become tangent to the saddle-node curve, and the system linearization has, simultaneously, a pair of purely imaginary eigenvalues plus one real eigenvalue at the origin. This bifurcation (rigorously studied in [44], [47]), does not introduce new bifurcations on the equilibrium points but generates additional bifurcation curves of limit cycles. The normal form coefficients are: $s = 1$, $\theta = -0.1855$ and $E_0 = -1$ (obtained with MatCont and following the notation in [44]). According to these values, in addition to the Hopf and saddle-node bifurcation curves, the unfolding of the corresponding normal form describes the birth and annihilation of a quasiperiodic orbit by means of a Neimark-Sacker and homoclinic bifurcation curves. Details on the emerging dynamics can be consulted in [22] where a singularity with the same normal form has been described on a nine bus power system. The numerical continuation of the Neimark-Sacker is a very difficult task considering the large dimension of the system. Therefore, only the corresponding bifurcation point (labeled NS) for $K_f = 140$ is depicted.

Near to the zero-Hopf singularity, the Hopf bifurcation curve H_1 undergoes a generalized Hopf (or Bautin) bifurcation, denoted as GH in Fig. 6(a). At this point the stability index of the Hopf branch changes from a positive value [subcritical Hopf H_1^+, solid line in Fig. 6(a)] to a negative one (supercritical Hopf H_1^-, dashed line). At the GH bifurcation point, a curve of saddle-node bifurcation of limit cycles emerges. The curve is not shown in the figure, for the same reason that restricts the continuation of the NS curve.

To show the ensemble of limit cycles organized around ZH and GH bifurcations, two horizontal slices (one-parameter bifurcation diagrams) for $K_f = 140$ and $K_f = 145$ are shown in Fig. 6(b) and (c), respectively. For $K_f = 140$, H_2^+ is subcritical, the corresponding cycle is unstable and emerges to the left. The cycle exhibits a Neimark-Sacker bifurcation for $\alpha_B = 1.3397$, as predicted by the normal form of the zero-Hopf bifurcation. At this point a torus or quasiperiodic oscillation arises. The cycle becomes stable and undergoes a cyclic-fold bifurcation CF (emerged at GH) for $\alpha_B = 1.3385$, where it collapses
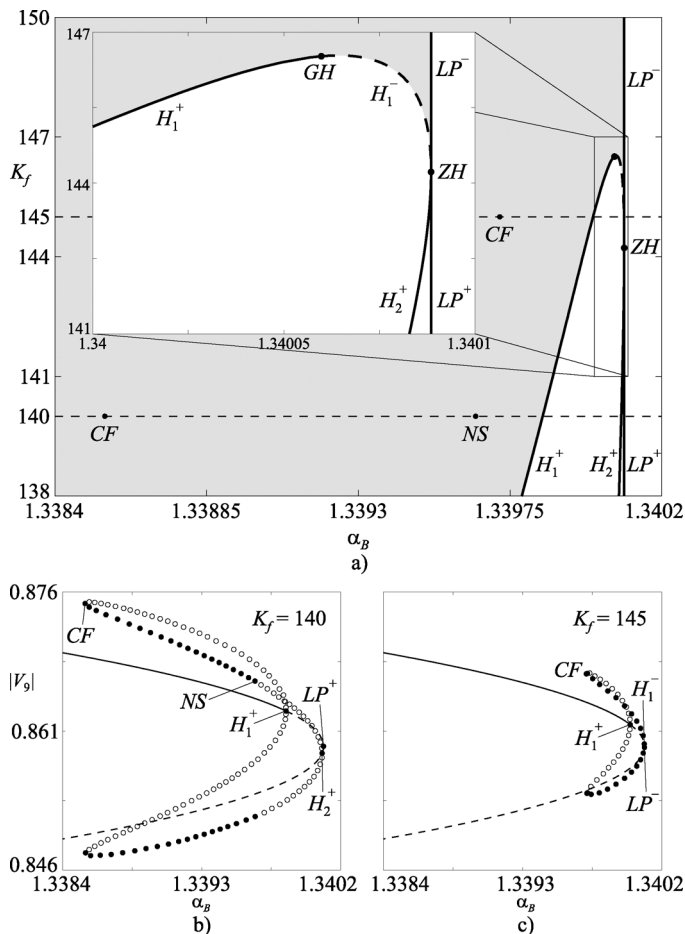
Fig. 6. (a) Blow-up of the two-parameter bifurcation diagram (rectangle in Fig. 5); (b) One-parameter bifurcation slice for $K_f = 140$; (c) One-parameter bifurcation slice for $K_f = 145$.

with the unstable cycle born at H_1^+. The dynamical scenario changes for $K_f = 145$ due to the zero-Hopf bifurcation. In this case, H_1^- is supercritical, the cycle emerges to the left, but it is stable. Then it collapses with the one born at H_1^+ in the cyclic fold bifurcation CF.

Notice that the escenario for $K_f = 140$, is similar to the one obtained with $K_f = 0$ [compare Figs. 6(b) and 4(a)]. The only difference is that for $K_f = 0$ the NS bifurcation is not present, and the cycle is always unstable. This bifurcation probably collapses at a strong 1:1 resonance[2] for $0 < K_f < 140$, and does not appear in the bifurcation diagram for $K_f = 0$. Therefore, the equilibrium point is stable on the gray area in Figs. 5 and 6(a), but it will be less robust to perturbations in the vicinity of the bifurcation curves.

A. Main Effect of the Controller on the Dynamics

Let us begin by describing the main effect of the controller on the bifurcation structure. To clarify the description, two additional one-parameter bifurcation diagrams for $K_f = 5/0.06$ and $K_f = 5/0.03$ are performed. The results are shown in Fig. 7(a) and (c), respectively. In the bifurcation diagram for $K_f = 5/0.06$ [Fig. 7(a)], the locus of the equilibria does not change from the open loop case (compare the solid and dashed

---

²The unfolding of the normal form of the 1:1 strong resonance can be consulted in [44]

lines with the ones in Fig. 4 for $K_f = 0$), since the transient frequency loop does not act on steady-state due to the washout filter. Thus, the saddle-node bifurcation LP remains without change, but the (dynamic) Hopf bifurcation H_1^+ is displaced towards the right, very close to LP. The case $K_f = 5/0.03$ [Fig. 7(c)] removes both Hopf bifurcations, thus the equilibrium point remains stable until it collapses in the bifurcation LP. In both cases, the intra-area modes move towards the right half plane as α_B is increased, but they remain well damped, as can be appreciated in the locus of Fig. 7(b) and (d). Nevertheless, the inter-area mode approaches the imaginary axis when α_B is increased. Notice that for $K_f = 5/0.03$ this mode does not cross the imaginary axis, since the Hopf bifurcation H_1^+ was removed, but it is poorly damped for values of α_B close to the saddle-node bifurcation.

A clear example of the stabilizing effect of the short-term frequency controller is depicted in Fig. 8, where a step variation of α_B from 1.25 to 1.31 is applied. Suppose that the system is operating in steady-state with $\alpha_B = 1.25$ without short-term frequency regulation (before H_1^+ in Fig. 4). Then, a step in the load B is performed and the loading factor changes to $\alpha_B = 1.31$, i.e., after H_1^+. At this point the system cannot find any stable equilibrium, resulting in an oscillatory transient that concludes in a voltage collapse event, as shown by the dashed curve in Fig. 8. When the short-term frequency controller is active the system supports the loading step and after an oscillatory transient converges to a new stable equilibrium. The cases with $K_f = 5/0.06$ and $K_f = 5/0.03$ are represented by the solid gray and solid black curves shown in Fig. 8, respectively.

B. Effect on the Frequency Regulation

The effect of this controller on the frequency regulation is illustrated by means of time-domain simulations for a 20% step change on load B (at bus 9 in Fig. 1) from the nominal operation point, i.e., $\alpha_B = 1$. The results are shown in Fig. 9, where dotted lines correspond to $K_f = 0$ (open loop), gray solid curves to $K_f = 5/0.06$ (6% short-term frequency droop) and black solid curves to $K_f = 5/0.03$ (3% droop).

In Fig. 9(a), the frequencies of the areas are represented by the average of the frequencies of its generators, i.e., generators on buses 1 and 2 for area #1, and buses 3 and 4 for area #2. The comparison among the curves shows that this simple control strategy not only improves the frequency regulation, decreasing the maximum frequency deviation (by 13% when using $K_f = 5/0.06$ or 24% for $K_f = 5/0.03$), but also provides additional damping to the inter-area oscillation. A practical range of local control time delay τ_f (varying from 10 to 200 ms) was analyzed and it was found that this parameter has no significative effect on the response of the controller.

The active power injected by the wind farm at the PCC (P_{12}) and the corresponding wind turbine speed (ω_t), are shown in Fig. 9(b) and (c), respectively. In the open loop case ($K_f = 0$), both the active power and the turbine speed are not affected by the load step. They remain constant at their optimal values, and the wind farm behaves as an independent active power source. On the other hand, when the transient frequency regulation is active ($K_f > 0$) and the load step is applied, the frequency deviation at the PCC is sensed and the wind farm starts to inject
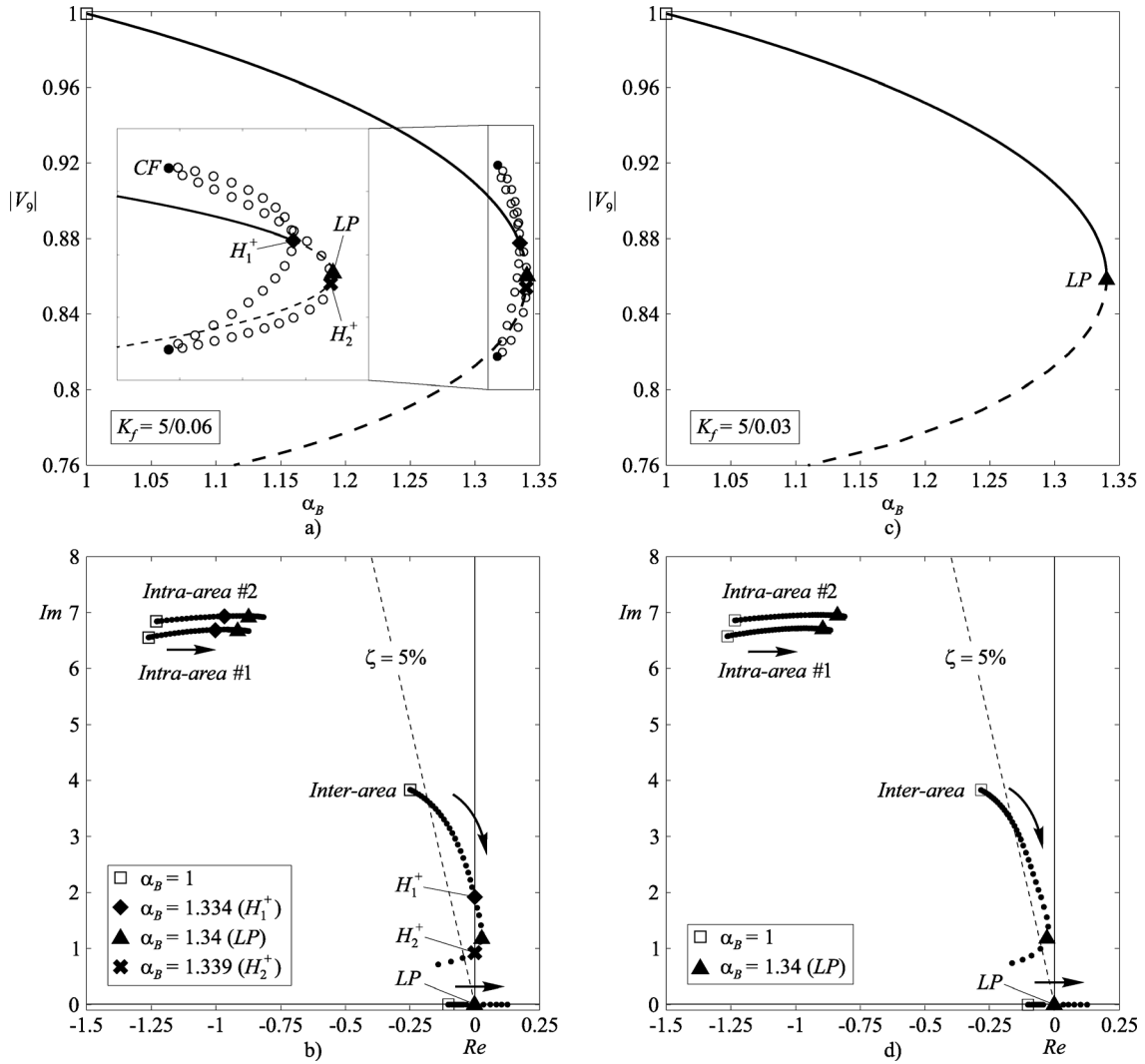
Fig. 7. Bifurcation diagrams with short-term frequency regulation. (a) Equilibria curve varying α_B, with $K_f = 5/0.06$. (b) Eigenvalues varying load B, with $K_f = 5/0.06$. (c) Equilibria curve with $K_f = 5/0.03$. (d) Eigenvalues corresponding to Fig. 7(c).
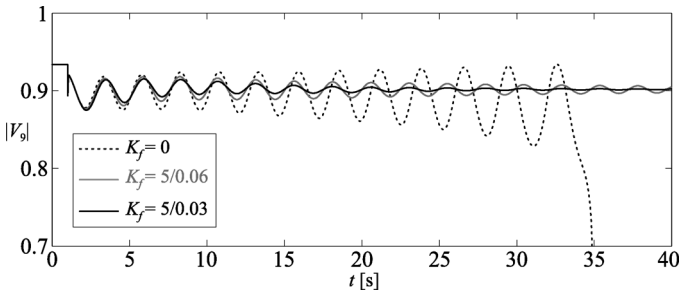

Fig. 8. Stabilizing effect of the short-term frequency controller. Response due to a step variation from $\alpha_B = 1.25$ to $\alpha_B = 1.31$, with $K_f = 0$ (dashed curve), $K_f = 5/0.06$ (solid gray) and $K_f = 5/0.03$ (solid black).

additional power in order to *transiently* compensate the generation/load unbalance. The additional energy is resorted to the kinetic energy stored in the rotating masses; hence, initially, the turbine speed decreases [as shown in Fig. 9(c)]. Then, the MPPT algorithm will slowly bring the turbine speed to its optimal value, and the energy extracted from the rotating masses is recovered. Similar results are obtained if the step is applied on the load of area #1 (load A on Fig. 1). The oscillatory response

seen in Fig. 9 corresponds to the poorly damped inter-area mode with frequency around 0.6 Hz. This is an important feature of the two-area system of Fig. 1, and its effects on the dynamics will be analyzed in the following.

V. ANALYSIS OF THE DYNAMICS INCLUDING THE INTER-AREA OSCILLATIONS COMPENSATOR

As shown in the previous section, the short-term frequency controller has a stabilizing effect on the inter-area mode. This mode can be further damped if a dedicated compensator is included in the wind farm. The strategy consists in measuring the frequencies of both areas, denoted as $\omega_{area\#1}$ and $\omega_{area\#2}$, and using them to modify the active power reference of the WECS (see Fig. 2). Since the areas can be distant from the wind farm, a communication time delay τ_ω will be considered in the measurement of frequencies. The effect of K_ω on the inter-area mode will be analyzed for different values of the time delay τ_ω and the loading factor α_B. The short-term frequency droop gain will be fixed at $K_f = 5/0.03$ [avoiding the Hopf bifurcations, see Figs. 5 and 7(c)].
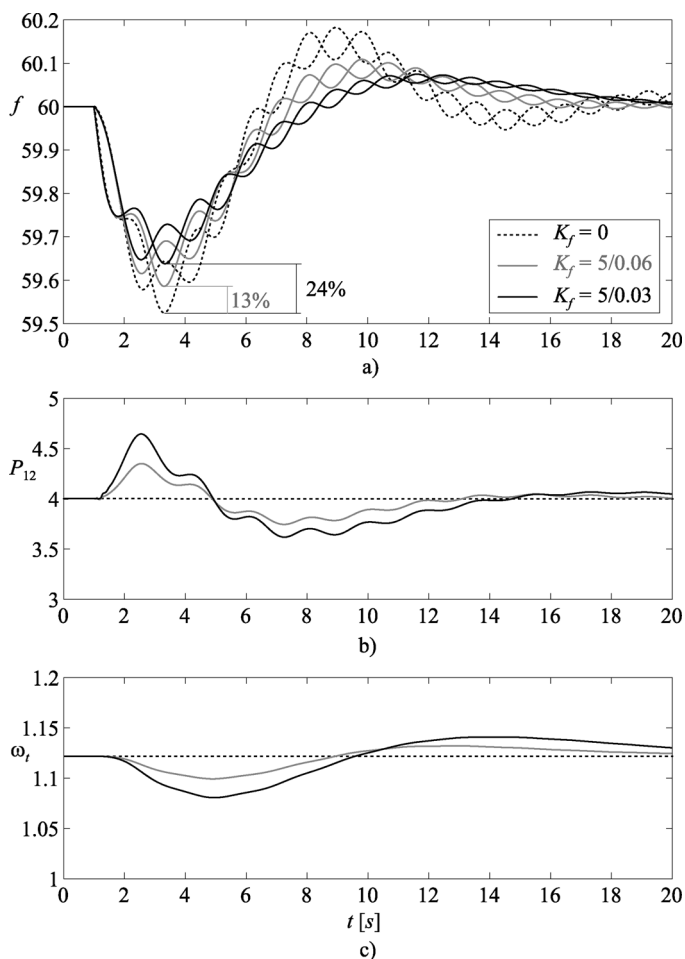
Fig. 9. Short-term frequency regulation for different gain values: $K_f = 0$ (dotted curves), $K_f = 5/0.06$ (solid gray), $K_f = 5/0.03$ (solid black). (a) Frequency variation due to a 20% step change in load B. (b) Active power injected by the WECS (P_{12}). (c) Wind turbine speed (ω_t).

TABLE I
PHASE COMPENSATOR PARAMETERS.

τ_ω	$(\omega_1 + \omega_2)/2 - (\omega_3 + \omega_4)/2$	$\omega_1 - \omega_3$
300 ms	$T_1=0.72$, $T_2=0.09$, $N=1$	$T_1=0.84$, $T_2=0.08$, $N=1$
500 ms	$T_1=0.65$, $T_2=0.1$, $N=2$	$T_1=0.7$, $T_2=0.096$, $N=2$

The analysis is carried out by performing numerical continuations varying α_B for different fixed values of K_ω. The value of the gain is selected in order to have a damping of 20% (approximately) on the inter-area mode for $\alpha_B = 1$. This methodology is repeated for two measurement time delays: $\tau_\omega = 300$ ms and $\tau_\omega = 500$ ms; and two sets of measured signals: using the frequency average of the generators in each area, $\omega_{area\#1} = (\omega_1 + \omega_2)/2$ and $\omega_{area\#2} = (\omega_3 + \omega_4)/2$, and using the frequency of a single generator per area $\omega_{area\#1} = \omega_1$ and $\omega_{area\#2} = \omega_3$. The phase compensator was designed using the residue method described in [48], resulting in the parameter values shown in Table I.

The results for $\tau_\omega = 300$ ms are shown in Fig. 10(a)–(c). The bifurcation diagram [Fig. 10(a)] remains without change from that shown in Fig. 7(c), due to the wash-out filter action.

This controller introduces a stabilizing effect that can be appreciated in the eigenvalue loci shown in Fig. 10(b)-(c) for $K_\omega = 0$ (without compensation) and $K_\omega = 135$ (a suitable choice, as explained below). In these figures the locations of eigenvalues for loading factors $\alpha_B = 1$, 1.25, 1.33 and 1.34 (the extreme value corresponding to the saddle-node bifurcation LP), are indicated. For both sets of measured signals, the main effect of K_ω is on the the real part of the inter-area mode. For $K_\omega = 0$ the damping of the inter-area mode for all practical loading cases ($\alpha_B = 1$ to 1.33) is around 5%, but for $K_\omega = 135$, it provides a damping of 15%–20%. As will be shown in simulations, this value produces a response without inter-area oscillations. Increasing K_ω produces an additional control effort from the WECS but does not represent a substantial improvement in the overall response.

For larger time delays, the bifurcation diagram does not change [Fig. 10(d)], but the performance of the compensator is slightly deteriorated as is depicted in Fig. 10(e)-(f) for $\tau_\omega = 500$ ms. With $K_\omega = 60$, a good damping factor between 10% and 20% can be obtained with both measured signals.

A. Main Effect of the Controller on the Dynamics

There is a couple of distinctive features of the inter-area damping controller. It neither modifies the equilibria nor introduces additional singularities, hence all the bifurcation diagrams are essentially the same [Fig. 10(a) and (d)]. In addition, this controller does not affect the intra-area modes when the measured signals are the frequency average of each area [Fig. 10(b) and (e)]. In this case the intra-area modes are "filtered" by the averaging procedure. This is not the case when a single frequency per area is used [Fig. 10(c) and (f)]. The effect can be seen in the variation on the intra-area mode in the area where the wind farm is connected. Nevertheless, this mode remains with an admissible damping and there are no other adverse phenomena on the remaining eigenvalues.

B. Effect on Inter-Area Oscillations

As in the case of the short-term frequency regulation, the performance of the inter-area mode compensator is tested for a 20% load step in load B. Fig. 11 shows the effect of the controller with $K_\omega = 135$, $\tau_\omega = 300$ ms (gray) and $K_\omega = 60$, $\tau_\omega = 500$ ms (black). In both cases, the measured signals are the average values of the frequencies of each area, i.e., $\omega_{area\#1} = (\omega_1 + \omega_2)/2$ and $\omega_{area\#2} = (\omega_3 + \omega_4)/2$. As shown in Fig. 11(a), the inter-area oscillation is practically eliminated, even when $\tau_\omega = 500$ ms (compare with the dotted curve for $K_f = K_\omega = 0$). The new compensator has a little effect on the short-term frequency regulation [compare Figs. 9(a) and 11(a)], since the controller only tries to reduce the differences between the frequencies of the areas and not the deviation from the nominal value. The active power generated by the WECS is shown in Fig. 11(b). The power available for the transient frequency regulation and the inter-area compensator is limited to ±20% of the WECS. The addition of the inter-area compensator does not represent a significant impact (besides an initial transient) on the wind turbine speed [compare Fig. 9(c) with Fig. 11(c)], since the speed deviation is mainly due to the short-term frequency
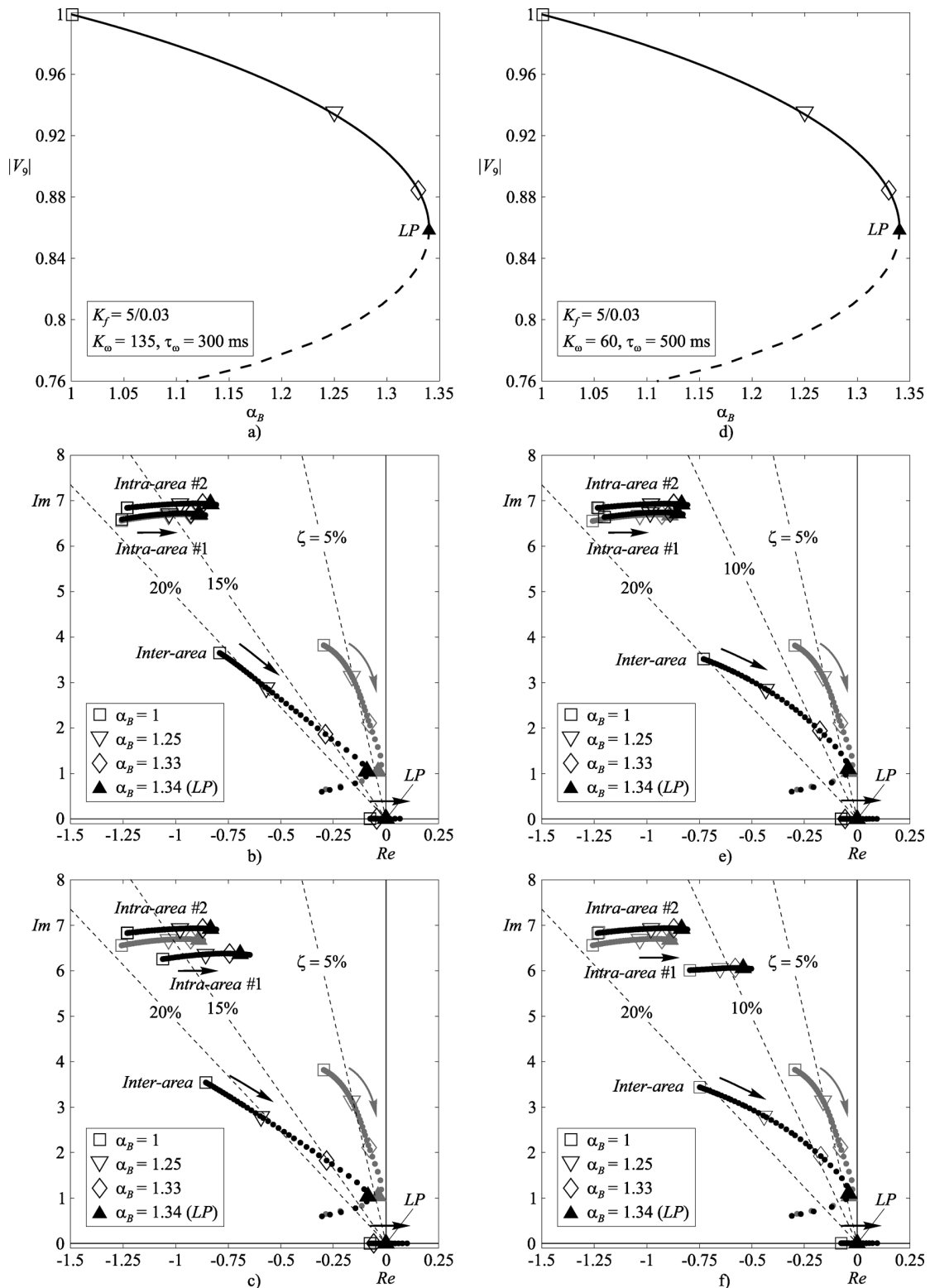
Fig. 10.   Effect of the inter-area compensator varying α_B for $K_f = 5/0.03$ and different time delays and measured signals. (a) Bifurcation diagram varying α_B with $K_\omega = 135$ and $\tau_\omega = 300$ ms. (b) Eigenvalues loci associated to Fig. 10(a), using the average frequencies as measurement inputs (gray: $K_\omega = 0$, black: $K_\omega = 135$). (c) Eigenvalues using a single frequency per area (gray: $K_\omega = 0$, black: $K_\omega = 135$). (d) Bifurcation diagram varying α_B with $K_\omega = 60$ and $\tau_\omega = 500$ ms. (e) Eigenvalues considering the average frequencies (gray: $K_\omega = 0$, black: $K_\omega = 60$). (f) Eigenvalues using a single frequency per area (gray: $K_\omega = 0$, black: $K_\omega = 60$).

controller. Time domain simulations were also performed using a single frequency per area, i.e., $\omega_{area\#1} = \omega_1$ and $\omega_{area\#2} = \omega_3$. The results are practically identical to the ones shown in Fig. 11.

VI.   ANALYSIS OF THE DYNAMICS INCLUDING THE VOLTAGE REGULATOR

The third additional controller of the WECS provides voltage support at the PCC. This compensator monitors the voltage
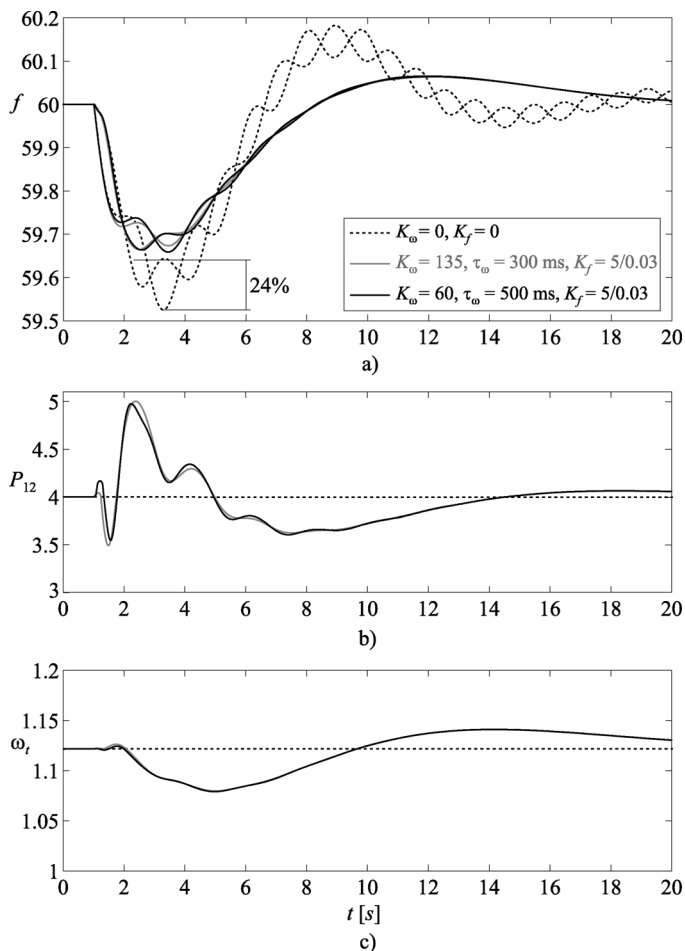
Fig. 11. Effect of the inter-area oscillation damping controller with both $K_\omega = 135$, $\tau_\omega = 300$ ms (solid gray) and $K_\omega = 60$, $\tau_\omega = 500$ ms (solid black). (a) Frequency variation due to a 20% step change in load B. (b) Active power injected by the WECS (P_{12}). (c) Wind turbine speed (ω_t).

Fig. 12. One-parameter bifurcation diagrams with voltage regulation (with $K_f = 5/0.03$ and $K_\omega = 135$). (a) Bifurcation diagrams varying α_B with $K_v = 5/0.05$ (black) and $K_v = 0$ (gray). (b) Loci of eigenvalues of Fig. 12(a).

error and modifies the reactive current reference (and therefore the reactive power) of the grid-side converter, according to the characteristic shown in Fig. 3. Unlike the previous controllers, the voltage compensator modifies the location of the saddle-node bifurcation. This is shown in the bifurcation diagram of Fig. 12(a), where the continuation for $K_v = 0$ is compared with the one for $K_v = 5/0.05$ (5% voltage droop). In both cases the gains of the transient frequency regulator and the inter-area compensator are fixed at $K_f = 5/0.03$ and $K_\omega = 135$, respectively.

The movement of the relevant eigenvalues is depicted in Fig. 12(b) for $K_v = 5/0.05$ (black dots) and compared with the ones with $K_v = 0$ (gray dots). It is important to notice that the voltage compensator provides a small additional damping to the inter-area mode and does not introduce an adverse affect on the other electromechanical modes of the system.

A. Main Effect of the Voltage Controller on the Dynamics

The voltage compensator moves the saddle-node bifurcation from $\alpha_B = 1.34$ ($K_v = 0$) to $\alpha_B = 1.392$ ($K_v = 5/0.05$) and does not add new dynamical phenomena. This is confirmed
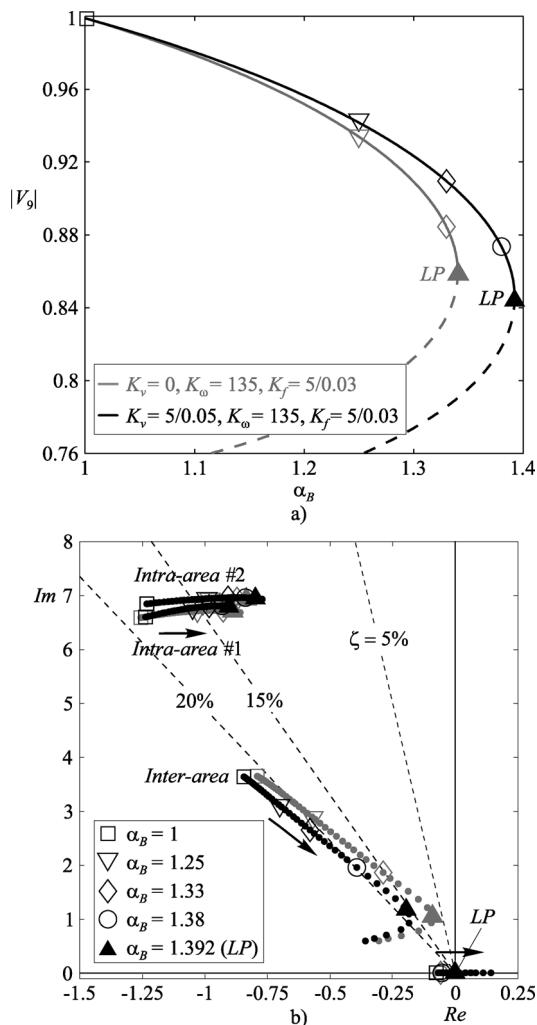

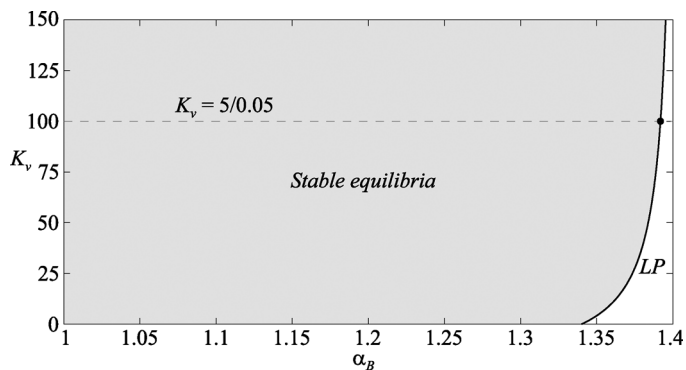Fig. 13. Saddle-node bifurcation curve varying α_B and K_v simultaneously.

by the two-parameter continuation in the parameter plane $\alpha_B - K_v$ shown in Fig. 13. The gray area shows how the stability region is extended by the controller. A further increase of K_v does not produce a significant change in the location of the saddle-node, since the curve becomes tangent to $\alpha_B \approx 1.4$.
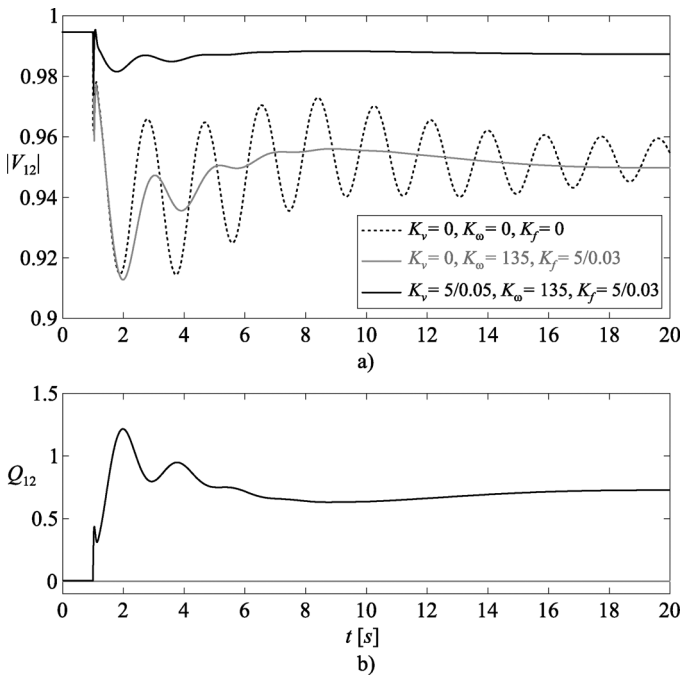
Fig. 14.   Effect of the voltage compensator due to a 20% load step. (a) Voltage regulation at bus 12 (PCC). (b) Reactive power injected by the wind farm.

B. Effect on Voltage Regulation

The performance of the controller is also investigated for a 20% step change in load B[3]. The response is shown in Fig. 14 (solid lines). For the sake of comparison, the responses corresponding to the open loop case ($K_v = K_f = K_\omega = 0$) and the one with the frequency regulation and inter-area compensators active ($K_f = 5/0.03$, $K_\omega = 135$, $K_v = 0$) are included. In the open loop case (dashed lines) the inter-area oscillation affects the voltage profile [Fig. 14(a)]. This effect is removed when the frequency regulation and inter-area compensators are activated (gray lines). Nevertheless, in both cases, there is no voltage regulation since the wind farm does not inject reactive power to the node [Fig. 14(b)]. When the corresponding controller is activated, voltage regulation is achieved as can be appreciated in Fig. 14(a) (solid black lines) for a 5% voltage droop ($K_v = 5/0.05$) and the two other compensators active ($K_f = 5/0.03$ and $K_\omega = 135$). In this case, the wind farm starts the injection of reactive current in order to compensate the voltage difference, resulting in a better voltage profile after the load step.

VII. CONCLUSIONS

The impact on the power system dynamics of a PMSG-based wind farm when performing ancillary services was investigated. A detailed bifurcation analysis was carried out in order to assess the effect of a set of control loops added to the WECS for: short-term frequency and voltage regulation, and inter-area oscillation damping. The preliminary analysis (without additional loops) revealed the presence of a Hopf bifurcation due to an inter-area mode and a saddle-node bifurcation. The bifurcation diagram varying the loading factor and the gain of the short-term frequency regulator shows that both singularities are unfolded by a zero-Hopf bifurcation (acting as organizing center). The short-term frequency regulator extends the stability region modifying the location of the Hopf curve, and for a suitable gain choice the Hopf bifurcation can be removed. On the other hand, the voltage regulator modifies the location of the saddle-node bifurcation, extending the stability region. Moreover, it improves the voltage profile without introducing adverse effects on the electromechanical modes. The analysis of the inter-area oscillation compensator shows that this mode can be practically eliminated from the response. The effects of the loading condition, the measured signals and the communication time delay were considered in the analysis. It was also shown that the use of the average value of the frequencies or a single one per area as control inputs produces similar effects on the inter-area mode, but the later strategy requires less measuring devices. Nevertheless, the single frequency approach may decrease the damping of the intra-area mode in the area where the wind farm is connected. In this analysis, an aggregated model of the wind farm was considered. This is a common approach for stability studies, but more realistic power systems are composed by several small wind farms. If they are connected to the same bus that the aggregated model, their power converters can control the individual power outputs in order to meet the desired target for the total output of the ensemble. Considering the proportional characteristic (*droop* control) of the short-term frequency and voltage regulators, the distributed topology of the wind farm should not have a significant impact on the bifurcation analysis. For the oscillation damping controller the situation is more complex, but the analysis can be extended following [41], where a decentralized compensator tuned for a modular WECS (e.g., one for each small wind power plant) is used, and concludes that practically the same results than a park-level compensator for the entire wind farm are obtained.

Real power systems have multiple areas with many generation and load centers and the interaction of the wind farm with the rest of the system is not straightforward. Nevertheless, the inclusion of additional controllers on variable-speed WECS expands the available options for controlling power system dynamics. These controllers will have a positive effect, provided that they are adequately tuned for the problem under consideration. The inter-area oscillation damping controller deserves particular attention since it introduces dynamics through a lead-lag compensation and a time delay from the remote measure. In addition, the mode controllability depends on the location of the wind farm. Generally, a modal analysis should be performed to determine which wind farms have more influence in the particular oscillatory mode of interest.

---

[3]A strategy that prioritizes the voltage support (reactive power injection) was implemented for the reference currents of the WECS converter. This scheme checks the maximum apparent current allowed, and reduces the active current reference if the limit is reached [10].

REFERENCES

[1] O. Anaya-Lara, N. Jenkins, J. Ekanayake, P. Cartwright, and M. Hughes*, Wind Energy Generation. Modelling and Control.* West Sussex, U.K.: Wiley, 2009.

[2] J. M. Carrasco, L. Garcia Franquelo, J. T. Bialasiewicz, E. Galván, R. C. Portillo Guisado, M. A. Martín Prats, J. I. León, and N. Moreno-Alfonso, "Power–electronic systems for the grid integration of renewable energy sources: A survey," *IEEE Trans. Ind. Electron.*, vol. 53, no. 4, pp. 1002–1016, Aug. 2006.

[3] M. Liserre, R. Cárdenas, M. Molinas, and J. Rodriguez, "Overview of multi-MW wind turbines and wind parks," *IEEE Trans. Ind. Electron.*, vol. 58, no. 4, pp. 1081–1095, Apr. 2011.

[4] D. Gautam, L. Goel, R. Ayyanar, V. Vittal, and T. Harbour, "Control strategy to mitigate the impact of reduced inertia due to doubly fed induction generators on large power systems," *IEEE Trans. Power Syst.*, vol. 26, no. 1, pp. 214–224, Feb. 2011.

[5] F. M. Hughes, O. Anaya-Lara, N. Jenkins, and G. Strbac, "Control of DFIG-based wind generation for power network support," *IEEE Trans. Power Syst.*, vol. 20, no. 4, pp. 1958–1966, Nov. 2005.

[6] G. Lalor, A. Mullane, and M. O'Malley, "Frequency control and wind turbine technologies," *IEEE Trans. Power Syst.*, vol. 20, no. 4, pp. 1905–1913, Nov. 2005.

[7] J. Morren, S. De Haan, W. Kling, and J. Ferreira, "Wind turbines emulating inertia and supporting primary frequency control," *IEEE Trans. Power Syst.*, vol. 21, no. 1, pp. 433–434, Feb. 2006.

[8] R. G. de Almeida and J. A. Pecas Lopes, "Participation of doubly fed induction wind generators in system frequency regulation," *IEEE Trans. Power Syst.*, vol. 22, no. 3, pp. 944–950, Aug. 2007.

[9] J. M. Mauricio, A. Marano, A. Gómez-Expósito, and J. L. Martínez Ramos, "Frequency regulation contribution through variable-speed wind energy conversion systems," *IEEE Trans. Power Syst.*, vol. 24, no. 1, pp. 173–180, 2009.

[10] K. Clark, N. W. Miller, and J. J. Sanchez-Gasca, "Modeling of GE wind turbine-generatorsfor grid studies, Version 4.5," General Electric International, Inc., Tech. Rep., 2010.

[11] G. Revel, A. E. Leon, D. M. Alonso, and J. L. Moiola, "Frequency regulation and inter-area oscillation damping using variable-speed wind generators," in *Proc. 6th IEEE/PES Transm. Distrib.: Latin America Conf. Expo. (T&D-LA)*, Motevideo, Uruguay, Sep. 3–5, 2012.

[12] F. M. Hughes, O. Anaya-Lara, N. Jenkins, and G. Strbac, "A power system stabilizer for DFIG-based wind generation," *IEEE Trans. Power Syst.*, vol. 21, no. 2, pp. 763–772, May 2006.

[13] L. Fan, H. Yin, and Z. Miao, "On active/reactive power modulation of DFIG-based wind generation for interarea oscillation damping," *IEEE Trans. Energy Convers.*, vol. 26, no. 2, pp. 513–521, Jun. 2011.

[14] H. G. Kwatny, R. F. Fischl, and C. O. Nwankpa, "Local bifurcation in power systems: Theory, computation, and application," *Proc. IEEE*, vol. 83, no. 11, pp. 1456–1483, Nov. 1995.

[15] W. Ji and V. Venkatasubramanian, "Dynamics of a minimal power system: Invariant tori and quasi-periodic motions," *IEEE Trans. Circuits Syst. I, Fundam. Theory Appl.*, vol. 42, no. 12, pp. 981–1000, Dec. 1995.

[16] W. D. Rosehart and C. A. Cañizares, "Bifurcation analysis of various power system models," *Int. J. Electr. Power Energy Syst.*, vol. 21, no. 3, pp. 171–182, Mar. 1999.

[17] I. Dobson, J. Zhang, S. Greene, H. Engdahl, and P. W. Sauer, "Is strong modal resonance a precursor to power system oscillations?," *IEEE Trans. Circuits Syst. I, Fundam. Theory Appl.*, vol. 48, no. 3, pp. 340–349, Mar. 2001.

[18] A. I. Zecevic and D. M. Miljkovic, "The effects of generation redispatch on Hopf bifurcations in electric power systems," *IEEE Trans. Circuits Syst. I, Fundam. Theory Appl.*, vol. 49, no. 8, pp. 1180–1186, Aug. 2002.

[19] A. A. Perleberg Lerm, C. A. Cañizares, and A. Silveira e Silva, "Multiparameter bifurcation analysis of the south Brazilian power system," *IEEE Trans. Power Syst.*, vol. 18, no. 2, pp. 737–746, May 2003.

[20] S. Ayasun, C. O. Nwankpa, and H. G. Kwatny, "Computation of singular and singularity induced bifurcation points of differential-algebraic power system model," *IEEE Trans. Circuits Syst. I, Reg. Papers*, vol. 51, no. 8, pp. 1525–1538, Aug. 2004.

[21] R. J. Avalos, C. A. Cañizares, F. Milano, and A. J. Conejo, "Equivalency of continuation and optimization methods to determine saddle-node and limit-induced bifurcations in power systems," *IEEE Trans. Circuits Syst. I, Reg. Papers*, vol. 59, no. 1, pp. 210–223, Jan. 2009.

[22] G. Revel, A. E. Leon, D. M. Alonso, and J. L. Moiola, "Bifurcation analysis on a multimachine power system model," *IEEE Trans. Circuits Syst. I, Reg. Papers*, vol. 57, no. 4, pp. 937–949, Apr. 2010.

[23] F. Milano and M. Anghel, "Impact of time delays on power system stability," *IEEE Trans. Circuits Syst. I, Reg. Papers*, vol. 59, no. 4, pp. 889–900, Apr. 2012.

[24] H. A. Pulgar-Painemal and R. I. Gálvez-Cubillos, "Limit-induced bifurcation by wind farm voltage supervisory control," *Elect. Power Syst. Res.*, vol. 103, pp. 122–128, 2013.

[25] V. Moreno-Font, A. El Aroudi, J. Calvente, R. Giral, and L. Benadero, "Dynamics and stability issues of a single-inductor dual-switching DC-DC converter," *IEEE Trans. Circuits Syst. I, Reg. Papers*, vol. 57, no. 2, pp. 415–426, Feb. 2010.

[26] F. Xie, R. Yang, and B. Zhang, "Bifurcation and border collision analysis of voltage-mode-controlled flyback converter based on total ampere-turns," *IEEE Trans. Circuits Syst. I, Reg. Papers*, vol. 58, no. 9, pp. 2269–2280, Sep. 2011.

[27] D. Giaouris, S. Banerjee, O. Imrayed, K. Mandal, B. Zahawi, and V. Pickert, "Complex interaction between tori and onset of three-frequency quasi-periodicity in a current mode controlled boost converter," *IEEE Trans. Circuits Syst. I, Reg. Papers*, vol. 59, no. 1, pp. 207–214, Jan. 2012.

[28] M. Huang, S.-C. Wong, C. Tse, and X. Ruan, "Catastrophic bifurcation in three-phase voltage-source converters," *IEEE Trans. Circuits Syst. I, Reg. Papers*, vol. 60, no. 4, pp. 1062–1071, Apr. 2013.

[29] K. Mandal, S. Banerjee, and C. Chakraborty, "Symmetry-breaking bifurcation in series-parallel load resonant dc-dc converters," *IEEE Trans. Circuits Syst. I, Reg. Papers*, vol. 60, no. 3, pp. 778–787, Mar. 2013.

[30] X. Xiong, C. Tse, and X. Ruan, "Bifurcation analysis of standalone photovoltaic-battery hybrid power system," *IEEE Trans. Circuits Syst. I, Reg. Papers*, vol. 60, no. 5, pp. 1354–1365, May 2013.

[31] D. Wei, B. Zhang, D. Qiu, and X. Luo, "Effects of current time-delayed feedback on the dynamics of a permanent-magnet synchronous motor," *IEEE Trans. Circuits Syst. II, Exp. Briefs*, vol. 57, no. 6, pp. 456–460, Jun. 2010.

[32] P. Kundur, *Power System Stability and Control*. New York: McGraw-Hill, 1994.

[33] W. Govaerts, Y. A. Kuznetsov, V. De Witte, A. Dhooge, H. G. E. Meijer, W. Maestrom, A. M. Riet, and B. Sautois, "MATCONT and CL-MATCONT: Continuation toolboxes in MATLAB," Gent University and Utrech University, Tech. Rep., 2011.

[34] W. D. Rosehart and C. A. Cañizares, "Elimination of algebraic constraints in power system studies," in *Proc. IEEE Can. Conf. Electr. Comput. Eng.*, May 1998, vol. 2, pp. 685–688.

[35] M. Ilić and J. Zaborszky, *Dynamics and Control of Large Electric Power Systems*. New York: Wiley, 2000.

[36] R. Pena, J. Clare, and G. Asher, "Doubly fed induction generator using back-to-back PWM converters and its application to variable-speed wind-energy generation," *IEE Proc. Elect. Power Appl.*, vol. 143, no. 3, pp. 231–241, May 1996.

[37] J. Slootweg, S. de Haan, H. Polinder, and W. Kling, "General model for representing variable speed wind turbines in power system dynamics simulations," *IEEE Trans. Power Syst.*, vol. 18, no. 1, pp. 144–151, Feb. 2003.

[38] J. Chow, J. Sanchez-Gasca, H. Ren, and S. Wang, "Power system damping controller design-using multiple input signals," *IEEE Control Syst.*, vol. 20, no. 4, pp. 82–90, Aug. 2000.

[39] D. Dotta, A. S. e Silva, and I. C. Decker, "Wide-area measurements-based two-level control design considering signal transmission delay," *IEEE Trans. Power Syst.*, vol. 24, no. 1, pp. 208–216, Feb. 2009.

[40] H. Huang and C. Chung, "Coordinated damping control design for DFIG-based wind generation considering power output variation," *IEEE Trans. Power Syst.*, vol. 27, no. 4, pp. 1916–1925, Nov. 2012.

[41] T. Knuppel, J. Nielsen, K. Jensen, A. Dixon, and J. Ostergaard, "Power oscillation damping capabilities of wind power plant with full converter wind turbines considering its distributed and modular characteristics," *IET Renewable Power Gener.*, vol. 7, no. 5, pp. 431–442, Sep. 2013.

[42] M. Tsili and S. Papathanassiou, "A review of grid code technical requirements for wind farms," *IET Renewable Power Gener.*, vol. 3, no. 3, pp. 308–332, Sep. 2009.

[43] J. Martínez, P. Kjaer, P. Rodriguez, and R. Teodorescu, "Design and analysis of a slope voltage control for a DFIG wind power plant," *IEEE Trans. Energy Convers.*, vol. 27, no. 1, pp. 11–20, 2012.

[44] Y. A. Kuznetsov, *Elements of Applied Bifurcation Theory*, 3rd ed. New York: Springer-Verlag, 2004.

[45] C. Vournas and N. Sakellaridis, "Region of attraction in a power system with discrete LTCs," *IEEE Trans. Circuits Syst. I, Reg. Papers*, vol. 53, no. 7, pp. 1610–1618, Jul. 2006.

[46] M. Anghel, F. Milano, and A. Papachristodoulou, "Algorithmic construction of Lyapunov functions for power system stability analysis," *IEEE Trans. Circuits Syst. I, Reg. Papers*, vol. 60, no. 9, pp. 2533–2546, Sep. 2013.

[47] J. Guckenheimer and P. Holmes, *Nonlinear Oscillations, Dynamical Systems, and Bifurcations of Vector Fields*. New York: Springer-Verlag, 1993.

[48] M. E. Aboul-Ela, A. A. Sallam, J. D. McCalley, and A. A. Fouad, "Damping controller design for power system oscillations using global signals," *IEEE Trans. Power Syst.*, vol. 11, no. 2, pp. 767–773, May 1996.

Gustavo Revel (S'08–M'10) received the B.S. degree in electronic engineering and the Ph.D degree in engineering from the Universidad Nacional del Sur (UNS), Bahía Blanca, Argentina, in 2005 and 2010, respectively. He is currently working at Departamento de Ingeniería Eléctrica y de Computadoras (UNS) and since 2012 he is also a member of CONICET (National Scientific and Technical Research Council—Argentina). His primary area of interest is nonlinear dynamics and bifurcation theory applied to electric power systems.

Andres E. Leon (S'05–M'13) was born in Argentina in 1979. He received the Electrical Engineering degree from Universidad Nacional del Comahue, Neuquén, Argentina, in 2005, and the Ph.D. degree from Universidad Nacional del Sur, Bahía Blanca, Argentina, in 2011. Since 2012, he has been Researcher of the National Scientific and Technical Research Council (CONICET), developing his work at the Research Institute of Electrical Engineering (Instituto de Investigaciones en Ingeniería Eléctrica "Alfredo Desages", IIIE), Bahía Blanca, Argentina. His primary areas of interest are power system control and wind energy conversion systems.

Diego M. Alonso received the degree in electronic engineering and the Ph.D. degree in control systems from the Universidad Nacional del Sur (UNS), Bahía Blanca, Argentina, in 1997 and 2002, respectively. Since 1997, he has been with the Departamento de Ingeniería Eléctrica y de Computadoras at UNS where he is Professor. He is also a member of the CONICET (National Council of Scientific Research of Argentina). His main research interest is in the field of nonlinear systems dynamics and control.

Jorge L. Moiola (SM'98) received the B.S. degree in electrical engineering from the Universidad Nacional del Sur (UNS), Bahía Blanca, Argentina, in 1986, the M.Sc. degree in electrical engineering from the University of Houston, TX, in 1991, and the Ph.D. degree from the UNS, in 1992. Since then, he has been with the Department of Electrical Engineering at UNS, where he is currently Associate Professor and a member of the CONICET (National Council of Scientific Research of Argentina). In 2001, he was a Research Scholar of the Alexander von Humboldt Foundation at the University of Cologne. Dr. Moiola was the Editor-in-Chief of the *Latin American Applied Research Journal* (1999–2005), Associate Editor of the IEEE TRANSACTIONS ON CIRCUITS AND SYSTEMS–II: EXPRESS BRIEFS (2004–2005) and currently he is Associate Editor of the *International Journal of Bifurcation and Chaos*. His primary research interest is in the field of nonlinear oscillations and bifurcations related to control systems theory.